paying part of the energetic cost of these induced changes, paromomycin facilitates the increased incorporation of amino acids from near-cognate tRNAs.

References and Notes

1. Reviewed in M. Ibba, D. Söll, *Science* **286**, 1893 (1999).
2. J. Davies, W. Gilbert, L. Gorini, *Proc. Natl. Acad. Sci. U.S.A.* **51**, 883 (1964).
3. J. J. Hopfield, *Proc. Natl. Acad. Sci. U.S.A.* **71**, 4135 (1974).
4. J. Ninio, *Biochimie* **57**, 587 (1975).
5. R. C. Thompson, P. J. Stone, *Proc. Natl. Acad. Sci. U.S.A.* **74**, 198 (1977).
6. T. Ruusala, M. Ehrenberg, C. G. Kurland, *EMBO J.* **1**, 741 (1982).
7. T. Pape, W. Wintermeyer, M. Rodnina, *EMBO J.* **18**, 3800 (1999).
8. ———, *Nature Struct. Biol.* **7**, 104 (2000).
9. M. Eigen, L. De Maeyer, *Naturwissenschaften* **53**, 50 (1966).
10. A. P. Potapov, *FEBS Lett.* **146**, 5 (1982).
11. ———, F. J. Triana-Alonso, K. H. Nierhaus, *J. Biol. Chem.* **270**, 17680 (1995).
12. R. C. Thompson, A. M. Karim, *Proc. Natl. Acad. Sci. U.S.A.* **79**, 4922 (1982).
13. D. Moazed, H. F. Noller, *J. Mol. Biol.* **211**, 135 (1990).
14. F. Mueller, H. Stark, M. van Heel, J. Rinke-Appel, R. Brimacombe, *J. Mol. Biol.* **271**, 566 (1997).
15. M. O'Connor *et al.*, *Biochem. Cell Biol.* **73**, 859. (1995).
16. F. Schluenzen *et al.*, *Cell* **102**, 615 (2000).
17. B. T. Wimberly *et al.*, *Nature* **407**, 327 (2000).
18. S. Yoshizawa, D. Fourmy, J. D. Puglisi, *Science* **285**, 1722 (1999).
19. D. Moazed, H. F. Noller, *Nature* **327**, 389 (1987).
20. D. Fourmy, M. I. Recht, S. C. Blanchard, J. D. Puglisi, *Science* **274**, 1367 (1996).
21. A. P. Carter *et al.*, *Nature* **407**, 340 (2000).
22. D. Fourmy, S. Yoshizawa, J. D. Puglisi, *J. Mol. Biol.* **277**, 333 (1998).
23. M. S. VanLoock, T. R. Easterwood, S. C. Harvey, *J. Mol. Biol.* **285**, 2069 (1999).
24. J. H. Cate, M. M. Yusupov, G. Z. Yusupova, T. N. Earnest, H. F. Noller, *Science* **285**, 2095 (1999).
25. A. P. Carter *et al.*, *Science* **291**, 498 (2001).
26. Crystals of the 30S subunit from *T. thermophilus* were grown as described (*17*). A $tRNA^{Phe}$ ASL corresponding to the sequence GGGGAUUGAAAAUCCCC, and the U_6 hexanucleotide were synthesized chemically. The ASL and U_6 hexanucleotide were purified by gel electrophoresis. Crystals were transferred to a stabilizing buffer containing 26% 2-methyl-2,4-pentanediol (MPD) as described (*17*). Soaks of equimolar ASL and U_6 were done at a concentration of 100 or 300 μM in the same stabilizing buffer, while paromomycin, if present, was at a concentration of 80 μM. Initial screening of crystals was done at beamlines 14.1 and 14.2 at the Synchrotron Radiation Source at Daresbury Laboratory (Warrington, UK), where a 3.8 Å resolution data set on one of the soaks was also collected. All data to high resolution were collected at beamline SBC-19ID at the Advanced Photon Source at Argonne National Laboratory (Illinois), integrated and scaled with HKL-2000 (*49*). The atomic structure of the 30S subunit (*17*), omitting various parts near the A site, was used as a starting point for refinement against the three data sets with CNS (*50*). Initially, rigid-body refinement was done with the domains of 16S RNA and the individual proteins as separate rigid objects. This was followed by positional refinement, simulated annealing with torsion angle dynamics, and then two rounds of grouped B-factor refinement and refinement of the occupancies of metal ions. The ASL (15 and 11 residues in the presence and absence of paromomycin, respectively), mRNA, and any changes in the 30S subunit were built into the density in difference Fourier maps with the program O (*51*) before a final round of refinement. Coordinates have been deposited in the Protein Data Bank with accession numbers 1IBK (30S/paromomycin), 1IBL (30S/ASL/U_6/paromomycin), and 1IBM (30S/ASL/U_6). Coordinates of individual components will be made available on http://alf1.mrc-lmb.cam.ac.uk/~ramak/30S.
27. H. Shi, P. B. Moore, *RNA* **6**, 1091 (2000).
28. L. Jovine, S. Djordjevic, D. Rhodes, *J. Mol. Biol.* **301**, 401 (2000).
29. Y. Goldgur *et al.*, *Structure* **5**, 59 (1997).
30. F. H. C. Crick, *J. Mol. Biol.* **19**, 548 (1966).
31. S. Yokoyama, S. Nishimura, in *tRNA: Structure, Biosynthesis and Function*, D. Söll, U. RajBhandary, Eds. (American Society for Microbiology, Washington, DC, 1995), pp. 207–223.
32. N. C. Seeman, J. M. Rosenberg, A. Rich, *Proc. Natl. Acad. Sci. U.S.A.* **73**, 804 (1976).
33. Reviewed in C. G. Kurland, D. Hughes, M. Ehrenberg, in Escherichia coli *and* Salmonella typhimurium; *Cellular and Molecular Biology*, F. C. Neidhardt *et al.*, Eds. (American Society for Microbiology, Washington, DC, ed. 2, 1996), vol. 1, pp. 979–1004.
34. T. Powers, H. F. Noller, *Proc. Natl. Acad. Sci. U.S.A.* **87**, 1042 (1990).
35. J. Cate *et al.*, *Science* **273**, 1696 (1996).
36. N. Ban, P. Nissen, J. Hansen, P. B. Moore, T. A. Steitz, *Science* **289**, 905 (2000).
37. P. Nissen, J. Ippolito, N. Ban, P. B. Moore, T. A. Steitz, *Proc. Natl. Acad. Sci. U.S.A.* (online), 10 April 2001.
38. E. A. Doherty, R. T. Batey, B. Masquida, J. A. Doudna, *Nature Struct. Biol.* **8**, 339 (2001).
39. S. Doublie, S. Tabor, A. M. Long, C. C. Richardson, T. Ellenberger, *Nature* **391**, 251 (1998).
40. J. R. Kiefer, C. Mao, J. C. Braman, L. S. Beese, *Nature* **391**, 304 (1998).
41. G. M. Cheetham, T. A. Steitz, *Science* **286**, 2305 (1999).
42. B. J. McCarthy, J. J. Holland, *Proc. Natl. Acad. Sci. U.S.A.* **54**, 880 (1965).
43. H. Stark *et al.*, *Nature* **389**, 403 (1997).
44. R. K. Agrawal *et al.*, *J. Cell Biol.* **150**, 447 (2000).
45. R. K. Agrawal *et al.*, *Science* **271**, 1000 (1996).
46. H. Stark *et al.*, *Cell* **88**, 19 (1997).
47. Supplementary data are available on *Science* Online at www.sciencemag.org/cgi/content/full/292/5518/897/DC1.
48. O. Piepenburg *et al.*, *Biochemistry* **39**, 1734. (2000).
49. Z. Otwinowski, W. Minor, in *Methods in Enzymology*, C. W. J. Carter, R. M. Sweet, Eds. (Academic Press, New York, 1997), vol. 276, pp. 307–325.
50. A. T. Brünger *et al.*, *Acta Crystallogr. D Biol. Crystallogr.* **54**, 905 (1998).
51. T. A. Jones, M. Kjeldgaard, *Methods Enzymol.* **277B**, 173 (1997).
52. R. Koradi, M. Billeter, K. Wüthrich, *J. Mol. Graphics* **14**, 51 (1996).

53. We thank S. Ginell and A. Joachimiak (APS) and M. MacDonald and E. Duke (Daresbury) for their help and advice with synchrotron data collection; P. Nissen for advice on making Fig. 3; and B. T. Wimberly and K. Nagai for comments on the manuscript. Supported by the Medical Research Council (U.K.) and grant GM 44973 from the NIH to S. W. White and V.R.. D.E.B. was the recipient of a Human Frontier Science Program postdoctoral fellowship.

12 March 2001; accepted 3 April 2001

Feynman's Path-Integral Approach for Intense-Laser–Atom Interactions

P. Salières,[1] B. Carré,[1] L. Le Déroff,[1] F. Grasbon,[2] G. G. Paulus,[2] H. Walther,[2] R. Kopold,[3] W. Becker,[3] D. B. Milošević,[4] A. Sanpera,[5] M. Lewenstein[5]*

Atoms interacting with intense laser fields can emit electrons and photons of very high energies. An intuitive and quantitative explanation of these highly nonlinear processes can be found in terms of a generalization of classical Newtonian particle trajectories, the so-called quantum orbits. Very few quantum orbits are necessary to reproduce the experimental results. These orbits are clearly identified, thus opening the way for an efficient control as well as previously unknown applications of these processes.

Quantum mechanics has been successful in explaining the physics of the microworld. Its standard mathematical formulation, which provides the basis for calculations of quantum-mechanical processes (*1*), requires a nearly complete break with classical intuition. In contrast, the alternative formulation of quantum mechanics developed by Feynman in terms of path integrals builds on the familiar Lagrangian concept of the action of an orbit in space and time and appears to be much closer to classical concepts (*2*). In Feynman's formulation, the probability amplitude of any quantum-mechanical process can be represented as a coherent superposition of contributions of all possible spatio-temporal paths that connect the initial and the final state of the system. The weight of each path is a complex number whose phase is equal to the classical action along the path. Even though this approach turned out to be very useful

[1]Centre d'Etudes de Saclay, CEA/DRECAM/SPAM, 91191 Gif-sur-Yvette, France. [2]Max-Planck-Institut für Quantenoptik, 85748 Garching, Germany. [3]Max-Born-Institut, 12489 Berlin, Germany. [4]Faculty of Science, University of Sarajevo, 71000 Sarajevo, Bosnia and Hercegovina. [5]Institute for Theoretical Physics, Universität Hannover, 30167 Hannover, Germany.

*To whom correspondence should be addressed. E-mail: lewen@itp.uni-hannover.de

in quantum field theory, it has, nevertheless, received much less practical use, due in part to the large number of different paths required to describe most phenomena (*3*).

Recently, the path-integral interpretation has set the frame for a unified view of the physics of nonlinear laser-atom interactions. Indeed, some phenomena that take place in intense fields (*4*) have only recently been partly elucidated. For example, in the process of above-threshold ionization (ATI) an atom may absorb many hundred more photons than necessary to get ionized, ejecting an electron of very high energy (*5*, *6*). Under the same conditions, the atom may emit photons having harmonic frequencies, that is, multiples of the incident-laser frequency ω. The harmonic frequencies can reach and exceed 300 ω and extend well into the water window (*7*, *8*), i.e., the region of the light spectrum between x-ray and ultraviolet (XUV) for which water is transparent. Such high-harmonic generation (HHG) is making available brilliant table-top sources of coherent XUV radiation, with pulse durations potentially in the sub-femtosecond regime (*9*). Other phenomena of interest are the nonsequential multiple ionization (creation of a multiply charged ion within a fraction of the laser-field period) (*10*, *11*) and photodetachment in external fields (*12*). The path integral formalism suggests we envision these processes in terms of "quantum orbits," i.e., space-time trajectories of the participating electrons. These quantum orbits have, however, imaginary parts related to tunneling ionization that determine the probability of the process. Quantum orbits have been able to explain subtle features of HHG (*13*) and ATI (*14*).

We report experimental and theoretical results that demonstrate the pervasive presence of quantum orbits as the basic building blocks for the probability amplitudes of these processes. Despite the complexity of the highly nonlinear laser-matter interaction, a very small number of clearly identified quantum orbits is sufficient to describe ATI or HHG processes. We observe the same type of orbits at work in ATI and HHG. Thus, in ATI spectra generated by a laser with elliptical polarization, each part of the spectrum can be attributed to one particular pair of quantum orbits. Moreover, we show how the contribution of a single quantum orbit can be isolated in phase-matched HHG, allowing for a direct measurement of the corresponding classical action. For both cases, we present experimental evidence in parallel with the theory. These experiments have pushed the present-day technology to its limits.

A description of ATI and HHG processes is given by the strong-field approximation (SFA) [for a review, see (*4*)]. This approximation assumes that the laser affects only weakly the states in which the electrons are strongly bound to the atomic nucleus. For the states in which the electrons are not bound to the nucleus, the effect of the binding potential is neglected, whereas that of the laser is fully considered. By the action of the laser field, an electron may be ionized at some time t_i and return to its parent ion at the later time $t_f = t_i + \tau$, where it may recombine with the ion emitting a photon of high energy (HHG) or rescatter (ATI of high order) and move out of the laser focus (*15*, *16*). For both HHG and high-order ATI (*17*), the probability amplitude M can be written in the form

$$M = \sum_n a_n \exp\{iS[\mathbf{r}_n(t)]/\hbar\} \qquad (1)$$

where a_n is an amplitude and S denotes the action. This corresponds indeed to Feynman's path integral, and the sum is, in fact, an infinite-dimensional functional integral. The SFA allows us to reduce it to a sum over a few quantum orbits, numbered by the subscript n. These are determined as follows: the total action $S[\mathbf{r}(t)]$ is the sum of three terms corresponding to the three steps mentioned above, $S[\mathbf{r}_n(t)] = S_{\text{bound},n}(t_{in}) + S_{\text{free},n}(t_{fn}, t_{in}) + S_{\text{final},n}(t_{fn})$. Here $S_{\text{bound},n}$, $S_{\text{free},n}$ and $S_{\text{final},n}$ denote the action of the bound electron, the ionized free electron, and the final action, respectively. The action of the bound electron is $S_{\text{bound},n} = -E_0 t_{in}$, with E_0 denoting the initial binding energy of the electron. The action $S_{\text{free},n}$ is calculated along the free-electron trajectory (the "quantum orbit")

$$m\mathbf{r}_n(t) = (t - t_{in})\mathbf{k}_n - e\int_{t_{in}}^{t} d\tau \mathbf{A}(\tau), (t_{in} \le t \le t_{fn}) \qquad (2)$$

where $\mathbf{k}_n$ refers to the electron's drift momentum after ionization and $\mathbf{A}(\tau)$ denotes the vector potential of the laser field. $S_{\text{bound},n}$ and $S_{\text{free},n}$ are the same for ATI and HHG processes [and for nonsequential multiple ionization, too (*18*)]. The final action for HHG corresponds to recombination and is given by $S_{\text{final},n} = (\hbar\omega_q + E_0)t_{fn}$. For ATI, the final action describes the outgoing electron and is calculated along a trajectory like Eq. 2, but with t_{in} and $\mathbf{k}_n$ substituted by t_{fn} and the final drift momentum $\mathbf{p}$ of the electron, respectively. In a semiclassical approximation, we can determine the parameters t_{in}, t_{fn}, and $\mathbf{k}_n$ by requiring the action to be stationary, which yields the following saddle-point equations

$$[\mathbf{k} - e\mathbf{A}(t_i)]^2 = 2mE_0 \qquad (3)$$

$$\mathbf{k}(t_f - t_i) = \int_{t_i}^{t_f} d\tau e\mathbf{A}(\tau) \qquad (4)$$

$$[\mathbf{k} - e\mathbf{A}(t_f)]^2 = \begin{cases} [\mathbf{p} - e\mathbf{A}(t_f)]^2 \text{ for ATI} \\ 2m(\hbar\omega_q + E_0) \text{ for HHG} \end{cases} \qquad (5)$$

This completes the reduction of the path integral to a sum over a few orbits.

The three above equations enforce energy conservation in the process of tunneling, return of the electron to the position from where it started, and energy conservation either when it rescatters into a state with the final (drift) momentum $\mathbf{p}$ or recombines to produce a harmonic photon with energy $\hbar\omega_q$, respectively. The solutions of the saddle-point equations are complex, because Eq. 3 cannot be satisfied for any real time ($E_0 < 0$). Hence, the orbits described by Eq. 2 are complex as well. The solutions can be ordered according to increasing travel time $\tau_n = t_{fn} - t_{in}$ so that $\tau_n < \tau_{n'}$ when $n < n'$. Equations 1 through 5 illustrate that the amplitude M is the coherent superposition of the contributions from these complex quantum orbits. In general, only those with travel times shorter than one or two periods of the field will make noticeable contributions to the sum described by Eq. 1.

Qualitatively different interference patterns occur, depending on how many and which trajectories are involved. For an experimental demonstration of the role of various orbits, the conditions should be chosen such that the contributions of different quantum orbits are easily distinguishable; i.e., they should appear in different energy regions and/or be of different strengths. This is most clearly observed in ATI experiments, which measure single-atom effects, and in particular with the use of an elliptically polarized laser field (*14*, *19*). In contrast to linear polarization, where the high-order ATI spectrum consists of one single plateau with its cutoff near 10 U_p (*5*, *6*) (U_p is the ponderomotive energy, proportional to I/ω^2, where I is the laser intensity), a staircase with several steps is observed for elliptical polarization. The results of such a measurement (Fig. 1) (*20*) display the rich structure of the spectrum predicted by the quantum-orbit approximation described by Eqs. 1 through 5 (*19*). The scheme of these theoretical predictions is represented by the straight lines.

The top step in the spectrum does not concern us here: it is made up by the "direct" electrons, i.e., those that leave the ion without rescattering. For the remaining steps, each can be attributed to the particular pairs of quantum orbits identified in the figure. The physical origin of the steps is as follows: in the process of tunneling, the electron most likely starts its orbit with zero velocity after

tunneling. For elliptical polarization, however, in order that such an orbit return to the parent ion, its starting velocity must be nonzero. The larger it is, the smaller the contribution of the associated orbit. Such is the case for the shortest orbits (depicted in blue), which require a particularly large starting velocity. Theory also predicts a small step (shown in green) in between the two main ones; the experimental data may show an indication of it.

Thus, elliptic polarization leads to a particular richness of the electronic quantum orbits and offers the possibility of microscopic control at the single-atom level of both ATI and HHG (*21*). Measured HHG, however, is generated by an ensemble of atoms. Therefore, it offers a unique possibility of macroscopic control of the emission and, thereby, of isolating the contribution of a single trajectory, as shown below. The HHG spectrum emitted by a single atom irradiated by a linearly polarized laser field exhibits a characteristic plateau for harmonic energies below $|E_0| + 3.2U_p$ and a rapidly decreasing cutoff region for higher energies. The upper-plateau region is dominated by the pair of orbits with the shortest and next-to-shortest travel times τ_1 and τ_2 (*15*–*17*), as similar to ATI (orbits drawn in dark and light blue). The contributions of these two trajectories to the atomic polarization have different laser-induced phases, related to the action accumulated along the orbit $\mathbf{r}_n(t)$ (n = 1,2) of Eq. 2. We can approximate the real part of this action, $\mathrm{Re}S_{\mathrm{free}}$, by the product $-U_p\tau_n$ of the ponderomotive energy by the travel time τ_n. The interference of the contributions of these two orbits results in an irregular single-atom HHG spectrum. However, the harmonic field measured in the experiments is the coherent addition of the fields produced by the different atoms. Efficient HHG requires phase matching of the harmonic field with the driving polarization.

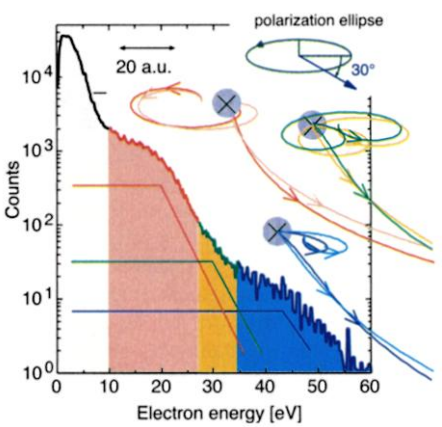

Fig. 1. ATI spectrum in xenon for an elliptically polarized laser field with ellipticity ξ = 0.36 and intensity 7.7 × 10^{13} W/cm^2 for emission at an angle with respect to the polarization axis as indicated. The different steps of the spectrum are shaded in different colors. For each step, the responsible quantum orbits, calculated from Eqs. 2 through 5, are displayed in shades of the same color. The crosses mark the position of the atom, and the length scale of the orbits is given in the upper left of the figure.

It has been shown recently that, in the case of a guided propagation, the atomic dispersion can compensate for the "geometric" dispersion (equivalent to the Gouy phase of a focused laser beam), resulting in good phase matching (*22*). If we focus a laser tightly into the atomic medium, the geometric dispersion is increased and no longer balanced by the atomic dispersion. However, now the laser-induced, position-dependent $U_p\tau$ phase of the atomic polarization is an important term involved in phase matching. In the longitudinal direction, this symmetric term (relative to the focus position) competes with the antisymmetric geometric phase. If we locate the atomic jet behind the focus, they may compensate each other if $U_p\tau$ does not vary too rapidly, i.e., for the τ_1 trajectory. Locating the atomic jet before or at the focus degrades phase matching on axis. However, it may lead to efficient phase matching off the propagation axis, provided the radial phase gradient is large enough and associated with the τ_2 trajectory. Thus, phase matching should provide a powerful mean to isolate and identify the contributions of the individual quantum orbits. Such macroscopic control of the coherence properties of HHG has been predicted in (*23*) and observed in spatial measurements.

Here, we concentrate on the spectral properties of the emission and show an unambiguous separation of the contributions from the two trajectories. Indeed, the laser-induced $U_p\tau$ phase inevitably leads to a phase modulation (chirp) of the harmonic emission because U_p is time-dependent after the laser envelope, such that the harmonic spectrum exhibits a signature of the τ_1 and τ_2 trajectories. At the same time, the experiments reported in (*24*, *25*) provide indirect signatures of quantum trajectories. In a series of recent experiments, however, we have accomplished a direct characterization of these trajectories.

The first experiment is complementary to the one of Bellini *et al.* (*13*), in which the spatial resolution of the contributions from the τ_1 and τ_2 trajectories was reported. We measured the distortion of the harmonic spectral profiles as a function of the jet-to-focus location, which acts as a phase-matching parameter (Fig. 2). This evolution can be explained within the frame of the above theory: the short τ_1 trajectory leads to a small, laser-induced chirp, i.e., a narrow harmonic spectrum (shaded in dark blue). Moving the atomic jet from after to before the focus gradually increases the contribution of the long τ_2 trajectory, which causes a larger chirp and, thus, a broader spectrum, shaded in light blue. Our experimental study ruled out other phenomena that can also induce a spectral distortion such as a blueshift of the laser frequency due to atomic ionization (*26*), self-phase modulation of the laser beam in the nonlinear medium, or any mechanism that only depends on the laser intensity. However, there is still a possibility that a temporal narrowing of the emission, e.g., due to transient phase matching, could induce such spectral broadening. To answer this question, we needed to measure jointly the temporal and the spectral profiles of the harmonic emission. This problem, which is particularly challenging for XUV pulses, was solved by coupling an XUV monochromator to an electron spectrometer (*27*). Both spectral width and pulse duration increase as the jet is moved from the after to before the focus (Fig. 3). Thus, we conclude that the spectral-width increase is indeed due to the laser-induced chirp, which varies with z along with the increasing contribution of the τ_2 trajectory (large chirp).

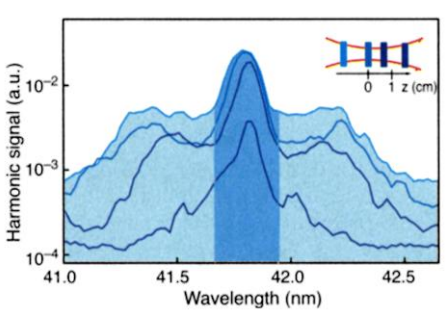

Fig. 2. Spectral profiles of the 19th harmonic generated in a 1-mm-long neon jet by a 130-fs 800-nm laser pulse focused (f/80) at 4 × 10^{14} W/cm^2. From bottom to top, the jet is moved from after to before the focus, as indicated in the inset. The color shades, light and dark blue, refer to the orbits of Fig. 1.

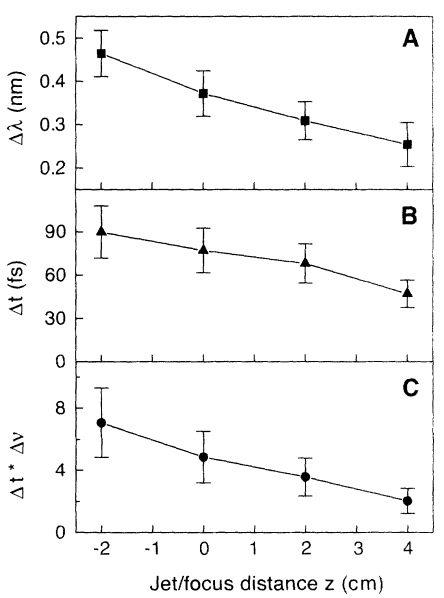

Fig. 3. (**A**) Spectral width Δλ, (**B**) pulse duration Δt, and (**C**) the product $\Delta t\,\Delta\nu$ for the 19th harmonic generated in argon as a function of the phase-matching parameter z. The 70-fs laser is focused to 2 × 10^{14} W/cm^2.

Accordingly, the product $\Delta t \Delta \nu$, which deviates largely from the Fourier transform limit, provides direct evidence of the laser-induced chirp. The experiment can be interpreted as a measurement of the action associated with the relevant electron trajectory; e.g., for the τ_1 trajectory, we find $\mathrm{Re}S_{\mathrm{free},1} = \alpha \times 10^{-14}$ $I[\mathrm{W/cm^2}]\hbar$ with $\alpha = 3 \pm 2$. The saddle-point Eqs. 3 through 5 yield, for the 19th harmonic at $I = 1.35 \times 10^{14}$ W/cm^2, $\alpha = 3.0$ ($\alpha = 22$) for the short (long) orbit, corresponding to $\tau_1 = 1.2$ fs and $\tau_2 = 2.2$ fs. These results agree nicely with accurate theoretical calculations (*28*).

Notwithstanding the combined complexities of atomic physics and nonlinear laser-matter interaction, HHG and ATI spectra can be reproduced with a small number of quantum orbits. The identification of these orbits and the measurement of the corresponding action offer a unique way of controlling these processes and opens the possibility of new applications.

References and Notes

1. C. Cohen-Tannoudji, B. Diu, F. Laloë, *Quantum Mechanics* (Wiley and Hermann, Paris, 1977).
2. R. P. Feynman, A. R. Hibbs, *Quantum Mechanics and Path Integrals* (McGraw-Hill, New York, 1965).
3. M. Gutzwiller, *Chaos in Classical and Quantum Mechanics* (Springer, Berlin, 1990).
4. K. Kulander, M. Lewenstein, *Atomic, Molecular, and Optical Physics Handbook*, G. W. Drake, Ed. (American Institute of Physics, Woodbury, NY, 1996), chap. 72, pp. 828–838.
5. G. G. Paulus, W. Nicklich, H. Xu, P. Lambropoulos, H. Walther, *Phys. Rev. Lett.* **72**, 2851 (1994).
6. B. Walker, B. Sheehy, K. C. Kulander, L. F. DiMauro, *Phys. Rev. Lett.* **77**, 5031 (1996).
7. Ch. Spielmann *et al.*, *Science* **278**, 661 (1997).
8. Z. Chang, A. Rundquist, H. Wang, M. M. Murnane, H. C. Kapteyn, *Phys. Rev. Lett.* **79**, 2967 (1997).
9. M. Drescher *et al.*, *Science* **291**, 1923 (2001); published online 15 February 2001 (10.1126/science.1058561).
10. Th. Weber *et al.*, *Nature* **405**, 658 (2000).
11. R. Moshammer *et al.*, *Phys. Rev. Lett.* **84**, 447 (2000).
12. H. C. Bryant *et al.*, *Phys. Rev. Lett.* **58**, 2412 (1987).
13. M. Bellini *et al.*, *Phys. Rev. Lett.* **81**, 297 (1998).
14. G. G. Paulus *et al.*, *Phys. Rev. Lett.* **84**, 3791 (2000).
15. K. C. Kulander, K. J. Schafer, J. L. Krause, in *Super-Intense Laser-Atom Physics*, B. Piraux, A. L'Huillier, K. Rzążewski, Eds. (Plenum, New York, 1993), pp. 95–110.
16. P. B. Corkum, *Phys. Rev. Lett.* **73**, 1994 (1993).
17. M. Lewenstein, Ph. Balcou, M. Yu. Ivanov, A. L'Huillier, P. B. Corkum, *Phys. Rev. A* **49**, 4998 (1994).
18. R. Kopold, W. Becker, H. Rottke, W. Sandner, *Phys. Rev. Lett.* **85**, 3781 (2000).
19. R. Kopold, D. B. Milošević, W. Becker, *Phys. Rev. Lett.* **84**, 3831 (2000).
20. The acquisition of a single spectrum requires the recording of up to a billion photoelectrons. Therefore, femtosecond lasers with extremely high repetition rates should be used, and the data acquisition must be able to handle electron count rates of 200 kHz and more. The laser system used for the ATI experiment delivers 50-fs pulses with a repetition rate of 100 kHz and intensities up to 3×10^{14} W/cm^2. The photoelectrons are recorded with a high-resolution time-of-flight spectrometer.
21. For the theory of HHG by an elliptically polarized laser field, see (*29*); for an early experiment, see (*30*). Similar control is offered by the use of multicolor fields or static magnetic fields; see, for instance (*31*).
22. A. Rundquist *et al.*, *Science* **280**, 1412 (1998).
23. P. Salières, A. L'Huillier, M. Lewenstein, *Phys. Rev. Lett.* **74**, 3776 (1995).
24. This laser-induced chirp can be compensated by the imposed chirp of the laser. Such control is demonstrated in (*32*).
25. Shaping the temporal envelope of the harmonic emission results in a corresponding shaping of the spectral profile; see (*33*).
26. C.-G. Wahlström, J. Larsson, A. Persson, T. Starczewski, S. Svanberg, *Phys. Rev. A* **48**, 4709 (1993).
27. The harmonics generated in an argon jet are sent into an XUV monochromator. By moving the grating in the first diffraction order and closing the exit slit, we measure a well-resolved spectrum. Then, the grating is set in the 0th order (so that the XUV pulse is not time-stretched), the slit is widely opened, and all the harmonic components are directed into a xenon gas target in the source volume of an electron spectrometer, together with a second laser beam, where they produce two-color ATI (harmonic + second laser with variable delay). The corresponding photoelectron lines provide the cross-correlation signal from which the harmonic pulse duration can be derived, as shown in (*34*).
28. M. B. Gaarde *et al.*, *Phys. Rev. A* **59**, 1367 (1999).
29. P. B. Corkum, N. H. Burnett, M. Y. Ivanov, *Opt. Lett.* **19**, 1870 (1994).
30. K. S. Budil, P. Salières, A. L'Huillier, T. Ditmire, M. D. Perry, *Phys. Rev. A* **48**, R3437 (1993).
31. D. B. Milošević, A. F. Starace, *Phys. Rev. Lett.* **82**, 2653 (1999).
32. Z. Chang *et al.*, *Phys. Rev. A* **58**, R30 (1998).
33. C. Altucci *et al.*, *Phys. Rev. A* **58**, 3934 (1998).
34. T. E. Glover, R. W. Schoenlein, A. H. Shin, C. W. Shank, *Phys. Rev. Lett.* **76**, 2468 (1996).

35. We thank the Deutsche Forschungsgemeinschaft, the Alexander von Humboldt-Foundation, the VolkswagenStiftung, and the European Union TMR networks ERBFMRX-CT96-0002 and ERB-FMRX-CT96-0087.

8 January 2001; accepted 20 March 2001

Density Fluctuations Under Confinement: When Is a Fluid Not a Fluid?

M. Heuberger,* M. Zäch, N. D. Spencer

Knowing the behavior of a fluid in small volumes is essential for the understanding of a vast array of common problems in science, such as biological interactions, fracture propagation, and molecular tribology and adhesion, as well as pressure solvation and other geophysical processes. When a fluid is confined, its phase behavior is altered and excluded-volume effects become apparent. Pioneering measurements performed with the surface forces apparatus have revealed so-called structural or oscillatory solvation forces as well as the occurrence of a finite shear stress, which was interpreted as a solidification transition. Here, we report measurements obtained with an extended surface forces apparatus, which makes use of fast spectral correlation to gain insight into the behavior of a thin film of cyclohexane confined within attoliter volumes, with simultaneous measurement of film thickness and refractive index. With decreasing pore width, cyclohexane is found to undergo a drastic transition from a three-dimensional bulk fluid to a two-dimensional adsorbate with strikingly different properties. Long-range density fluctuations of unexpected magnitude are observed.

Several experimental techniques, such as the surface forces apparatus (SFA) (*1*), differential scanning calorimetry (DSC) (*2*), neutron diffraction (*3*), or nuclear magnetic resonance (*4*) in porous materials, are capable of measuring properties of a fluid under molecular-level confinement. Here, an extended surface forces apparatus (eSFA) (*5*) has been used, comprising two thin (2 to 5 μm) mica sheets, which form a well-defined, single-slit pore of controllable width (i.e., surface separation), D (Fig. 1). The same mica sheets also form an optical interferometer using a 55-nm, silver-mirror coating on their reverse sides. The interferometer is immersed in a fluid, such as cyclohexane, and the fluid is increasingly confined between the surfaces by reducing D. Cyclohexane becomes the central optical layer of a multilayer interferometer, which selectively filters (infrared-free) white light in transmission. When the optical distance, $\Omega = D \cdot n$ (D = film thickness, n = refractive index), of the thin film varies, the condition for constructive interference is altered, and the wavelength shift of interference fringes with different chromatic orders can be measured. Odd- and even-ordered fringes shift differently as a function of n, an effect that allows D and n to be independently determined. As one would expect, the measurement of n is more difficult for thinner films (*5–7*). Our measurement errors are $\sigma_D < 25$ pm for distance and $\sigma_n < 0.05$ for refractive index. Detailed error calculations are available (*5*). This represents a 10- to 30-fold improvement over conventional SFA techniques (*6–12*). Using imaging optics, transmitted light from a spot of lateral diameter ø ~ 1 μm can be analyzed. For a very thin slit

Laboratory for Surface Science and Technology, ETH Zentrum, CH-8092 Zürich, Switzerland.

*To whom correspondence should be addressed. E-mail: heuberger@surface.mat.ethz.ch